Paper published in
2025 Supercond. Sci. Technol. 38 025012
DOI 10.1088/1361-6668/adaaa7

Design rules to scale-up magnetic screens made of bulk superconductors and closed-loop coated conductors: modelling and experiments

N. Rotheudt[1], J.-F. Fagnard[1], T. Hlasek[2,3], J. Plechacek[2] and P. Vanderbemden[1]

[1] Department of Electrical Engineering and Computer Science, Montefiore Institute B28, University of Liège, B-4000 Liège, Belgium.

[2] CAN SUPERCONDUCTORS, s.r.o., Ringhofferova 66, 251 68 Kamenice, Czech Republic

[3] Department of Inorganic Chemistry, University of Chemistry and Technology Prague, Technická 5, 166 28 Prague 6, Czech Republic

E-mail: nicolas.rotheudt@uliege.be

December 2024

Abstract. Hybrid magnetic screens combining a disk-shaped high-temperature superconducting bulk with closed-loop coated conductors have been recently demonstrated to significantly overcome the screening properties of a single bulk. The purpose of the present work is to investigate how to scale up these hybrid screens, i.e. further increase the field attenuation and widen efficiently the screened region using more closed-loop coated conductors. First of all, an axisymmetric finite element model using the Gmsh and GetDP environments with the $H - \phi$ formulation is implemented and used to study the influence of physical and geometrical parameters of the screens. The results show that the low-field screening factor SF and the screened surface area are strongly dependent on the geometry while having large J_c materials is mandatory to maintain the screening properties up to high fields. An important design rule is that the spacing between the concentric loops should be sufficiently small, which we explain physically by analysing the different paths followed by the flux lines. Then, experiments are carried out in liquid nitrogen (77 K) with $GdBa_2Cu_3O_7$ samples. Mapping the three components of the flux density above the screens subjected to an inhomogeneous applied field gives the following key results. First, the combination of the bulk with four loops spaced as recommended by the numerical model allows the screened surface area (SF $>$ 2) to be multiplied by ~ 9 with respect to the bulk alone. Second, reducing the asymmetry of the practical structure by flipping over some of the loops is highly beneficial for improving the screening properties: the maximum SF at 5.7 mm the bulk is measured to be multiplied by 1.6 without any additional superconductor. Importantly, the design rules obtained from both the numerical model and the experiments can be further extended and applied to various geometries or sizes of hybrid superconducting screens.

1. Introduction

Large inhomogeneous magnetic fields extending over wide surface areas are present in many engineering applications using superconductors: particle accelerators [1–4], high-power density rotating electric machines [5–9], current transformers [10], space applications [11] or magnetic resonance imaging (MRI) magnets [12, 13]. These applications often have a significant low-frequency stray field. Equipment sensitive to the magnetic field (e.g. cryocoolers) requires this stray field to be screened. In terms of systems used to reduce the stray field, one can distinguish between magnetic 'shields' and 'screens'. The term 'shields' usually refers to closed or partly closed geometries (e.g. a long tube or a vessel) and small volumes. On the opposite, magnetic screens deal with open geometries and large surfaces. This work focuses on the requirements to build efficient magnetic screens.

Ideally, a magnetic screen should fulfil three properties that are schematically illustrated and indicated in figure 1.

(i) The screen should provide a very strong field attenuation. The flux density measured behind the screen should be much smaller than the applied field that would exist without the screen.

(ii) The screen should act over wide surface areas or volumes. The spatial extension of the attenuation of the flux density brought by the screen should be as large as possible, i.e. the screened region should be maximized.

(iii) The screen should maintain its screening properties up to the highest possible applied fields. Even if the applied field increases, the screening effect should ideally not degrade.

Conventional ferromagnetic materials fail to fulfil the third property, as they are limited by their saturation magnetization ($\mu_0 M_{\text{sat}} \approx 0.7$ T for mu-metal [14]). This saturation prevents them for being used with the increasingly higher fields involved in engineering applications. On the opposite, superconductors do not suffer from this limitation. When subjected to a low-frequency (quasi-static) varying magnetic field, lossless current loops are induced within the material and 'passive' screening naturally appears [15–17]. Within superconductors, magnetic screens using high-temperature superconductors (HTS) can be operated well above the liquid helium temperature. Currently, three types of magnetic screens can be used against fields extending over wide surface areas: (1) bulk superconductors, (2) second generation (2G) coated conductors or (3) hybrid screens combining both.

First, bulk superconductors can be used to achieve

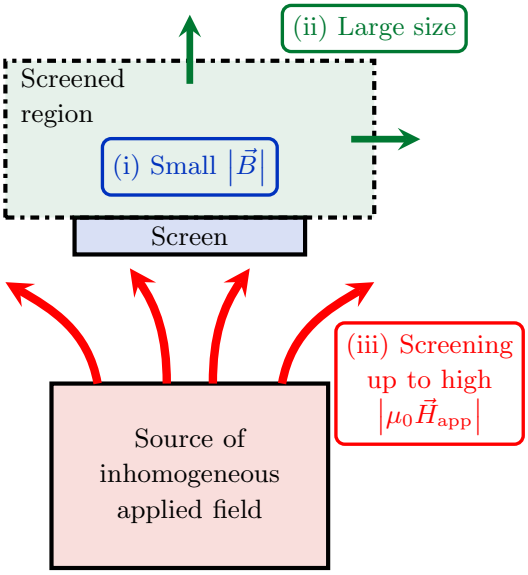

Figure 1. Schematic illustration of the three properties that an ideal screen should fulfil.

very efficient magnetic shielding or screening. Possible materials include MgB_2 [18–20], Bi-based superconductors [21, 22] or large grain (RE)$Ba_2Cu_3O_7$, where (RE) denotes a rare earth [23–26]. The limitation is that growing large (more than a few cm^2) bulk HTS plates remains a challenge. Hence, a possible solution to screen large surface areas is to arrange side-by-side several bulks. Several layers of bulks may be required to mitigate the presence of gaps between them [27–30].

Second, HTS coated conductors can be considered. One method to use them as magnetic screens is to build naturally short-circuited 'eye-shaped' loops in which persistent currents are induced [31,32]. The absence of resistive soldering allows quasi-static ('DC') fields to be screened. Large surface areas can be screened as these closed-loop coated conductors are naturally scalable.

Third, hybrid superconducting screens can be created by combining small bulks with naturally scalable closed-loop coated conductors. In a previous work, we studied the DC screening ability of these hybrid screens combining a disk-shaped bulk with coaxial closed-loop coated conductors [33]. We demonstrated that the maximum field attenuation obtained with these hybrid screens is roughly doubled with respect to the maximum attenuation of a bulk alone. Additionally, the surface area over which this attenuation is effective was multiplied by a factor 4.

Based on the promising results obtained with hybrid screens [33], this paper focuses on the design and the construction of large hybrid superconducting screens subjected to a DC inhomogeneous applied field. In this framework, several metrics can be defined in order to quantify the properties mentioned above.

(i) The field attenuation can be measured by the screening factor SF, defined locally as

$$\mathrm{SF}(\vec{r},\mu_0\vec{H}_{\rm app}) = \frac{\left|\mu_0\vec{H}_{\rm app}(\vec{r})\right|}{\left|\vec{B}(\vec{r},\mu_0\vec{H}_{\rm app})\right|}, \qquad (1)$$

where $\mu_0\vec{H}_{\rm app}$ is the inhomogeneous applied field (without the screen), $\vec{B}$ the flux density measured with the screen and $\vec{r}$ the position. Note that for these first two quantities, $\left|\vec{B}\right| = \sqrt{B_x^2+B_y^2+B_z^2}$. The definition of the screening factor is similar to that of the shielding factor. For the closed or partly closed geometries used in shielding, SF above 10^4 can be obtained [22, 34]. However, for magnetic screens dealing with open geometries, these high SF values are impossible to reach at a reasonable distance (i.e. a few mm) from the screen.

(ii) The spatial extension of the screened region can be defined as the region for which $\mathrm{SF} > \mathrm{SF}^*$, where SF^* is a certain threshold that can be defined depending on the application. In this paper, $\mathrm{SF}^* = 2$, corresponding to a 50 %-attenuation.

(iii) The field $\mu_0 H^*_{\rm app}$ up to which the screening properties are maintained should be defined with respect to the SF at virtually zero field, in practice measured at very low field. As the applied field increases, SF then decreases. The threshold field $\mu_0 H^*_{\rm app}$ is defined as the applied field for which the SF at a given position $\vec{r}_0$ is reduced to α times the maximum SF at $\vec{r}_0$, i.e.

$$\mathrm{SF}\left(\vec{r}_0,\mu_0 H^*_{\rm app}\right) = \alpha\,\mathrm{SF}\left(\vec{r}_0,\mu_0 H_{\rm app}\to 0\right). \qquad (2)$$

In this paper, $\alpha = 0.75$ is chosen arbitrarily and the value of the very low applied field ($\mu_0 H_{\rm app} \to 0$) is taken as the lowest accessible value, either simulated or measured.

In this paper, we explain numerically and demonstrate experimentally how to carefully design and build hybrid superconducting screens that are significantly scalable in terms of the three metrics defined above. In section 2, we present both methods used in this work, i.e. the finite element model and the experimental set-up. Then, we use the finite element model in section 3 to explain how the physical parameters of the screen affect the screening properties. We also describe how to choose the general geometrical parameters to optimize the design of the screen. Finally, in section 4, we carry out experiments demonstrating that the screened surface area can be easily extended by following the design rules detailed in section 3. In

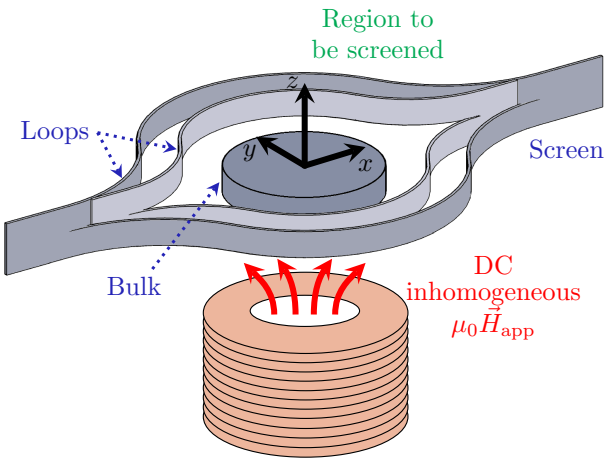

Figure 2. Schematic illustration of the typical geometry of the hybrid superconducting screens studied experimentally in this work.

addition, we explain why the intrinsic asymmetry of the closed-loop coated conductors is detrimental for the screening properties and implement experimentally an easy solution to overcome this limitation.

2. Methods

Hybrid superconducting screens are studied experimentally as well as numerically, using a simplified finite element (FE) model.

2.1. Experimental set-up

The typical geometry studied in this work is schematically shown in figure 2. The hybrid superconducting screen consists of a disk-shaped bulk and several closed-loop coated conductors. In this work, a single-domain melt-textured GdBCO/Ag ($GdBa_2Cu_3O_7$ + 0.4 mol Gd_2BaCuO_5 + 10% Ag_2O) bulk is used. This bulk sample is produced by the SDMG ('single-direction melt growth') method [35–37] at CAN Superconductors, s.r.o. The disk has a thickness of 5 mm, a diameter of 30 mm and a uniform critical current J_c around 200 A mm^{-2}. The closed-loop coated conductors are created by milling a slit in the middle of a tape segment and extending both parts of the loop around a cylindrical holder. In the following, the 'diameter of the loop' refers to the outer diameter of the underlying cylindrical holder. This structure allows persistent currents to flow [38–43]. In this work, the loops are obtained from a 10 mm-wide 2G GdBCO tape from Shanghai Superconductor Technology. The critical current is around 500 A at 77 K (self-field). In practice, the equivalent total supercurrent flowing in a loop is increased by superimposing several non-insulated layers (2 or 4) of similar closed-loop coated conductors.

The experimental set-up is the same as that described in our previous work [33]. This experimental set-up allows the screening properties of different hybrid screens to be measured. The superconducting samples are placed coaxially on 3D-printed sample holders. The top surface of the bulk is at the same height as the slit of the loops, which corresponds to $z = 0$ in the following. The superconducting screen is placed above a source coil generating the DC inhomogeneous field, as shown schematically in figure 2. The three components of the flux density in the region above the screen ($z > 0$) are measured simultaneously using a bespoke 3-axis Hall probe attached to a micro-displacement system. This 3-axis cryogenic Hall probe was designed in a previous work [44]. The Hall probe consists of a room-temperature 3-axis Hall sensor placed inside a G10 insert. The temperature of the inner part of the insert is controlled to be kept around room temperature when the insert is immersed in liquid nitrogen. As a result, the active area of the Hall sensor (corresponding here to a 250 µm-radius circle) is located at 2.2 ± 0.25 mm from the bottom surface of the insert, which determines the minimal distance from the bulk at which measurements can be performed. In practice, the results of this paper will be shown at $z = 5.7$ mm above the top surface of the bulk, i.e. when the bottom of the G10 insert of the Hall probe is 3.5 mm above the bulk. The typical uncertainty associated with the measurements of the Hall sensor is around ±100 µT.

The experimental process is similar for all the configurations investigated in this paper. First, the entire structure is cooled down to 77 K in a liquid nitrogen bath, without applied field. Once the temperature is stable, a DC current of 0.1 A is injected in the coil. Then, we wait for at least 5 minutes in order to ensure that the results are sufficiently time-independent, i.e. that two successive mappings of the flux density do not show any difference exceeding the typical uncertainty of the Hall sensor [33]. This waiting time also ensures that no 'coupling' currents appearing during the transient processes could flow between the non-insulated tapes, as it could be the case in AC regime [45]. Next, the spatial evolution of B_x, B_y and B_z is measured as described here above. After 30 minutes, the injected current is increased by 0.1 A and the waiting and measurement phases are repeated. The maximum injected current is 0.5 A, for which the inhomogeneous field produced by the source coil reaches around 100 mT at the bottom surface of the bulk, in absence of superconductors.

2.2. Simplified FE model

A finite element (FE) model is developed using the Gmsh and GetDP environments with the Life-HTS toolkit [46]. The exact geometry of hybrid screens is rather complex and has no symmetry axis because of the vertical shift between both parts of the loop and the 'eye' shape (see figure 2). Still, most of the properties can be physically understood thanks to a simplified model assuming axisymmetry. The main advantage is that this model can be run rapidly in 2D.

The geometry of the model is shown in figure 3. The axial direction is z and the transverse direction is y to be consistent with the experiments. The source coil generating the magnetic field to be screened is modelled as a single-turn inductor (in red in figure 3), i.e. a current is imposed externally in a homogenized version of the coil in which the different turns are not modelled. The hybrid screen consists of a disk-shaped bulk with N_L concentric superconducting loops. The distance between each loop is s_L. The dimensions of the bulk are $h_B = 5$ mm and $r_B = 15$ mm, as in the experiments. The height of the loop is $h_L = 5$ mm, which corresponds to the effective width of the practical closed-loop coated conductors (10 mm divided by 2). The loops are placed at the same height as the bulk, while there is the vertical offset between both halves of the loops in the experiments. Also, the thickness of the loops is artificially increased to $t_L = 1$ mm to ease the meshing of the domains. The mesh is structured and recombined in the superconductors and in the coil. The resolution uses the $H - \phi$ formulation [47, 48]. The current injected in the coil increases linearly with time and the current density is uniform within the coil region at all times. The classic power law [49] with $n = 40$ and a constant critical current density $J_c = 200$ A mm^{-2} (except in section 3.1) are used for all the superconductors. At the field levels investigated in this paper, the influence of the n value or a field-dependent J_c on the modelled SF was checked to be negligible.

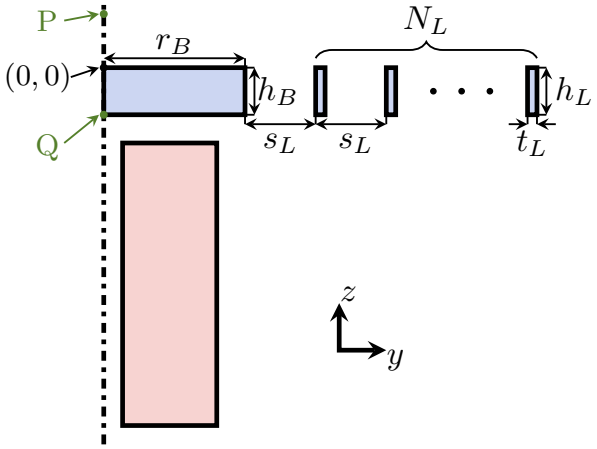

Figure 3. Schematic representation of the geometry studied in the FE model. The N_L superconducting loops of thickness t_L are separated by s_L. h_B and h_L are the heights of the bulk and the loops, respectively. The radius of the bulk is r_B. The source coil, in red, is modelled as a single-turn inductor. P and Q are two reference positions used in the section 3.1.

3. Numerical results and interpretation

Despite its simplicity, the finite element model can be used to draw meaningful conclusions on the influence of some physical and geometrical parameters on the screening properties. This section is subdivided into three parts. First, the influence of the critical current density J_c of the superconductors on the screening properties is shown. Second, the influence of the number and the positioning of the loops is studied. Finally, numerically calculated flux lines are shown to explain physically the influence of the position of the loop in the simplified case where a single loop is considered.

3.1. Influence of the critical current density

In order to understand how the critical current density affects SF, a screen with the 30 mm-diameter bulk and a single 50 mm-diameter loop is considered, i.e. $N_L = 1$ and $s_L = 10$ mm (see figure 3). Figure 4**(a)** shows the evolution of SF at 5.7 mm above the centre of the bulk (point P in figure 3) for different values of J_c. J_c^B stands for the critical current density of the bulk and J_c^L for the loop; both of them are expressed in A mm^{-2}. The evolution is shown as a function of the applied field at the centre of the bottom surface of the bulk, i.e. $(y, z) = (0, -5)$ [mm] (point Q in figure 3).

The first observation is that SF decreases when the applied field increases. Also, for all values of J_c, the initial SF is the same. This observation has practical implications on the design of superconducting screens. In section 1, it was mentioned that an ideal screen should provide (i) a large SF (ii) extending over large surface areas and (iii) up to high applied fields. The numerical results show that the maximum SF (at low field) is purely limited by the geometry, no matter how large J_c is. A large J_c, though, is very important for point (iii): the larger J_c, the slower the SF decrease, hence the larger the threshold field $\mu_0 H^*_{app}$ (as defined by (2)).

The previous observation can be explained as follows. For very small applied fields, the superconductors are almost not penetrated. Hence, in first approximation, they act as diamagnetic materials expelling the flux

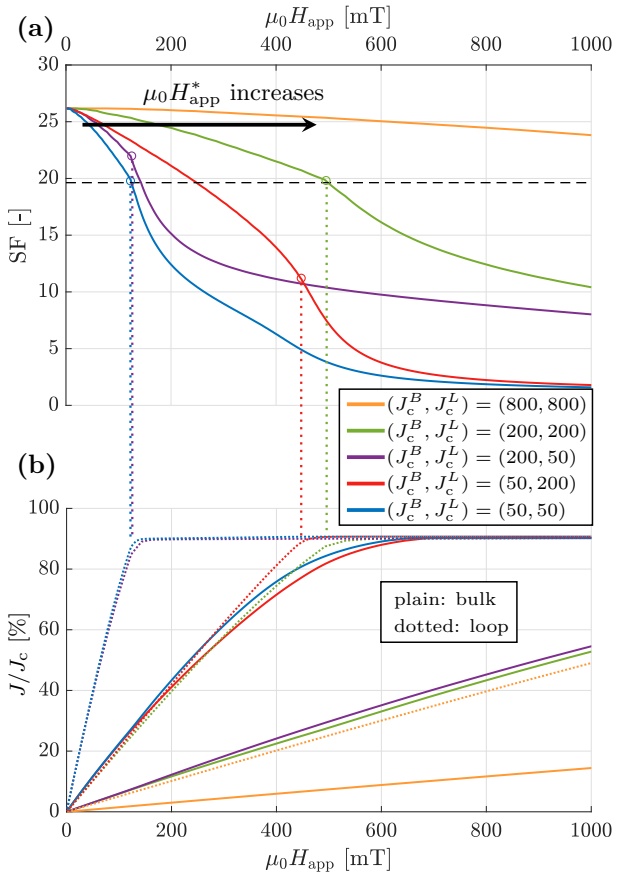

Figure 4. **(a)** Evolution of SF at $(y, z) = (0, 5.7)$ [mm] (point P) as a function of the applied field at $(y, z) = (0, -5)$ [mm] (point Q), i.e. at the bottom surface of the bulk. Five hybrid screens with the 30 mm-diameter bulk and a single loop of diameter 50 mm ($N_L = 1$, $s_L = 10$ mm) are considered for different values of the critical current density J_c^B in the bulk and J_c^L in the loop. The values in the legend are given in A mm^{-2} and are common to both figures. The horizontal dashed black line corresponds to $\alpha\,\mathrm{SF}\,((0, 5.7)[\mathrm{mm}], \mu_0 H_{app} \to 0)$, with $\alpha = 0.75$, as defined in (2). **(b)** Evolution of the average current density in the superconductors over the whole cross-section, divided by the corresponding critical current density, as a function of the applied field at $(y, z) = (0, -5)$ [mm]. The screens and the colours correspond to those in **(a)**. J_c^B is shown in plain lines and J_c^L in dotted lines.

lines [33]. The flux lines are diverted by the bulk close to the closed loops, i.e. exactly where the loops can oppose them at best. This is because the opposite field generated by the induced supercurrents is maximum close to the surface of the superconducting loops. Therefore, as long as the superconductors roughly act as diamagnetic materials, the screening properties are purely dependent on the path followed by the flux lines (see section 3.3), i.e. on the geometry. The flux lines are organized depending on the size of the bulk, the spacing between the loops, the number of loops and other geometric parameters of the screen. This reasoning is valid only if the superconductors are very weakly penetrated. As soon as the maximum current is induced in the loops, they cannot further oppose the increasing applied field. Similarly, when the bulk is penetrated through the lateral edges, the flux lines reach more and more easily the region to be screened and SF drops. The applied field for which this penetration is not negligible depends thus strongly on J_c.

Interestingly, the orange curve in figure 4**(a)**, for $J_c^B = J_c^L = 800$ A mm^{-2}, maintains an SF ~ 24 up to an applied field around 1 T, i.e. above the saturation of conventional mu-metal screens. These J_c values can easily be obtained in practice by lowering the operating temperature down to, for example, 20 K. This observation gives a hint on the ability of these hybrid screens to overcome ferromagnetic screens. Hence, the design rules obtained in this work may hold at lower temperature and higher applied fields provided that the superconductors remain weakly penetrated.

Besides these general observations, the evolution of J_c^B and J_c^L can be seen in figure 4**(b)**. It shows the average current density in the superconductors over the whole cross-section, divided by the corresponding J_c. This normalized quantity is an image of how much the superconductors are penetrated. Each colour corresponds to a different screen and, for each screen, the normalized critical current densities are shown separately for the bulk (plain lines) and the loop (dotted lines). Figure 4**(b)** illustrates that the average current density increases almost linearly with the applied field until it reaches its maximum value. Note that the maximum value obtained for all simulations is here $\sim 10\%$ smaller than J_c because of the small sweep rate of the applied field. The consequence of a small sweep rate is that the electric field induced in the superconductors is very small compared to $E_c = 1$ µV cm^{-1}, the classical threshold electric field used for defining J_c.

Combining both figures, several observations can be made and explained. First, the larger the J_c^L, the slower the initial decrease in SF, which indicates that the loop is the first element of the screen to saturate. It is confirmed by figure 4**(b)**, where the dotted lines (loop) always reach their maximum before the plain lines (corresponding bulk).

Second, the slope of SF exhibits a sudden change (marked by the circles in figure 4**(a)**). This slope change has a physical meaning: it corresponds to the field for which the loop starts to saturate (see figure 4**(b)**), such that the decrease in SF becomes suddenly faster when the applied field increases.

Third, once the loop is saturated, the behaviour of the screen is almost independent on J_c^L. The larger J_c^B, the better the overall behaviour of the screen at high

fields (e.g. for $\mu_0 H_{\rm app} > 600$ mT).

Fourth, once the superconductors are fully penetrated (blue and red curves for $\mu_0 H_{\rm app} > 600$ mT), SF keeps decreasing with $\mu_0 H_{\rm app}$. This is expected since, starting from (1) particularized at $(y, z) = (0, 5.7)$ [mm], where the field is purely axial,

$$\mathrm{SF}(\mu_0 H_{\rm app}) = \frac{\mu_0 H_{\rm app}}{B(\mu_0 H_{\rm app})} = \frac{\mu_0 H_{\rm app}}{\mu_0 H_{\rm app} - B_{\rm ind,max}}, \quad (3)$$

where $B_{\rm ind,max}$ is constant when the superconductors are fully penetrated: it is the maximum opposite field that can be induced by the screen at this position.

Fifth, while the loop and the bulk were discussed independently here above, relevant information regarding their coupling can be obtained by comparing the red and green dotted curves in figure 4**(b)**. It can be seen that the loop is saturated slightly faster when $J_{\rm c}^{\rm B}$ is small, even if $J_{\rm c}^{\rm L}$ is the same. This can be understood as follows. If $J_{\rm c}^{\rm B}$ decreases, the penetration front is deeper in the bulk for a given applied field. Consequently, the effective radius of the bulk is smaller and the flux embraced by the loop is larger. This is due to the fact that less flux lines are diverted outside the loop, as will be illustrated in section 3.3. The flux being larger for a given loop, the induced current density is larger and the loop saturates faster.

3.2. Influence of the geometry of the screen

The results obtained in section 3.1 showed that the initial SF is limited by the geometry of the screen and that the threshold field $\mu_0 H^*_{\rm app}$ depends strongly on $J_{\rm c}$. In this section, the critical current density is kept constant ($J_{\rm c}^{\rm B} = J_{\rm c}^{\rm L} = 200$ A mm^{-2}). The focus is therefore on understanding how the geometry of the screen influences the screening properties for $\mu_0 H_{\rm app} \ll \mu_0 H^*_{\rm app}$ (as defined by (2)). The goal is to design screens with a large screening factor SF extending over wide surface areas. For a given bulk, the two main parameters that can easily be adjusted are the number of loops N_L and the spacing s_L between them.

Figure 5**(a)** shows the spatial distribution of SF along y, at $z = 5.7$ mm, for three screens with different N_L. For all the screens, $s_L = 7.5$ mm. Also, the extension of the screened region SF > 2 is illustrated by the rectangles at the top of the figure. The hatched black rectangles are located at the positions of the superconductors. These numerical results are shown for very small applied fields, around 1 mT at the bottom surface of the bulk. The reason is to observe the 'ideal' behaviour of the screen, which is mainly geometrical, i.e. before penetration occurs.

The first observation is that SF peaks above the centre of the screen, decreases when approaching the extremity of the bulk ($y = 15$ mm) and increases again above the loops. Then, for a given appropriate spacing s_L, the larger N_L, the better the screening properties (both the maximum SF at $y = 0$ mm and the spatial extension). For example, the screen with $N_L = 4$ and $s_L = 7.5$ mm (red) is better than $N_L = 2$ and $s_L = 7.5$ mm (blue): the maximum SF is around 100 instead of 50 and the screened surface area is roughly 2.1 times larger.

In figure 5**(b)**, three hybrid screens made of four loops with different spacing s_L are compared in terms of SF at $z = 5.7$ mm. It can be observed that, for a given N_L, the screening properties depend much on the spacing s_L. For example, when $s_L = 12.5$ mm (green), the spatial extension is maximum while SF above the centre of the bulk is much smaller than for $s_L = 7.5$ mm (red), for which the screened region is less extended. Also, the maximum SF is almost the same for $s_L = 2.5$ mm and $s_L = 12.5$ mm. Consequently, the evolution of the screening properties with s_L is clearly non-monotonic.

This non-monotonic effect of s_L on the maximum SF is illustrated in figure 5**(c)**, which shows SF at $(0, 5.7)$ [mm] as a function of s_L, for different N_L. The three main observations made from these results are as follows. First, for a given s_L, the larger N_L, the larger SF. Second, for large s_L, the relative improvement brought by the addition of larger loops is very small. Last, for a given N_L, SF as a function of s_L exhibits a maximum, as suggested in figure 5**(b)**. For a given N_L, the maximum SF is obtained around $s_L = 7.5$ mm (between 5 and 7.5 mm for $N_L = 4$). Although this exact value depends on the characteristics of the source coil and the geometric parameters of the screen, the non-monotonic influence of s_L arises from the intrinsic geometry of hybrid screens and is expected to exist irrespectively of the particular dimensions of the source coil.

3.3. Flux lines and interpretation

Figure 5 highlighted that s_L has a non-monotonic influence on the maximum SF. This section aims at explaining physically why such a behaviour occurs. In order to keep the explanation as simple as possible, a hybrid screen with a single loop is considered.

Maximizing the screening factor SF above the centre of the screen means that the number of flux lines reaching this region should be minimized. The reason is that SF is inversely proportional to the flux lines density. Provided that $\mu_0 H_{\rm app} \ll \mu_0 H^*_{\rm app}$, the superconductors are very weakly penetrated and roughly behave as diamagnetic materials. Hence, the flux lines have to

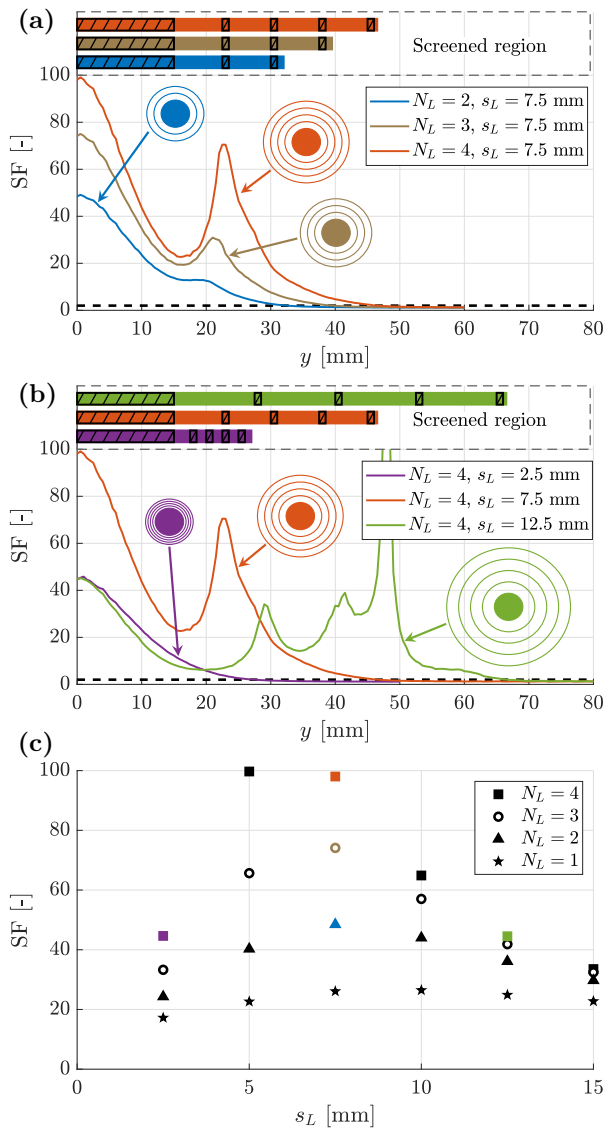

Figure 5. **(a)** Spatial distribution of SF along y, for $z = 5.7$ mm. These numerical results are shown for very small applied fields, around 1 mT at the bottom surface of the bulk. The rectangles at the top of the graph indicate in each case the spatial extension of the region SF > 2. The limit SF* $= 2$ is shown by a dashed black line. The hatched black parts inside the coloured rectangles are located at the positions of the superconductors. The small drawings illustrate (to scale) a top view of the different considered screens. **(b)** Same as figure 5**(a)** but for other screens. **(c)** SF at $(0, 5.7)$ as a function of s_L, for different N_L. Again, these numerical results are shown for an applied field around 1 mT at the bottom surface of the bulk. The coloured symbols correspond to the five configurations shown in **(a)** and **(b)**.

meander around them and the different possible paths should be investigated.

Numerically computed flux lines are illustrated in figure 6. Figure 6**(a)** and **(b)** are the numerical results for $s_L = 2.5$ mm and $s_L = 12.5$ mm, respectively, when a small applied field of around 1 mT is applied at the bottom surface of the bulk. Figure 6**(c)** is a schematic illustration of the two paths that can exist for the flux lines: between the bulk and the loop (path I), and all around the loop (path II).

The first observation is that when s_L is very small (figure 6**(a)**), the flux lines need to meander around the whole screen (path I). It can be explained intuitively: if the spacing between the loop is infinitely thin, the screen resembles very much a bulk of radius $r_B + s_L + t_L \approx r_B$ (see figure 3). In this extreme case, no flux line can go through path II.

Secondly, as s_L increases, another path exists for the flux lines (path II): some of them can leak through the gap between the bulk and the loop. It can be understood that for even larger s_L, almost all the flux lines go through this path II.

These two observations explain why an optimal SF can always be found for intermediate values of s_L. For infinitely small s_L, the screening properties are roughly those of a bulk alone. On the opposite, if the spacing s_L is infinitely large, the loop has no influence on the screening properties above the bulk and the screen also resembles a bulk alone. For intermediate s_L, there exist two competing phenomena giving rise to screening properties that overcome those of a bulk alone. These competing phenomena can be expressed as follows: increasing s_L reduces the contribution of I to the flux density above the screen but increases the contribution of II. An optimal screen should therefore use an intermediate s_L minimizing the sum of I and II.

The explanation above, regarding the paths for the flux lines for one single loop, can be extended for additional loops. The same compromise exists in the choice of s_L between each loop: a small spacing minimizes the flux lines leaking between the bulk and the first loop or between the loops but allows for many flux lines to go all around the screen; a large spacing leads to many flux lines leaking between the bulk and the loops. This also explains why increasing N_L for large s_L is not very useful (see figure 5**(c)**). When s_L is very large, most flux lines go between the bulk and the smallest loop or between the two smallest loops. Hence, adding, for example, a fourth loop brings only a tiny difference in SF above the centre.

In summary, in spite of its simplicity, the finite element model allows for several conclusions and design rules to be established. First, using top-quality superconductors with large critical current density does not increase the maximum SF that can be obtained. A large J_c, however, is crucial to withstand high applied fields. Second, the geometry of the screen limits the maximum SF. Understanding the different paths of the flux lines strongly help optimize the

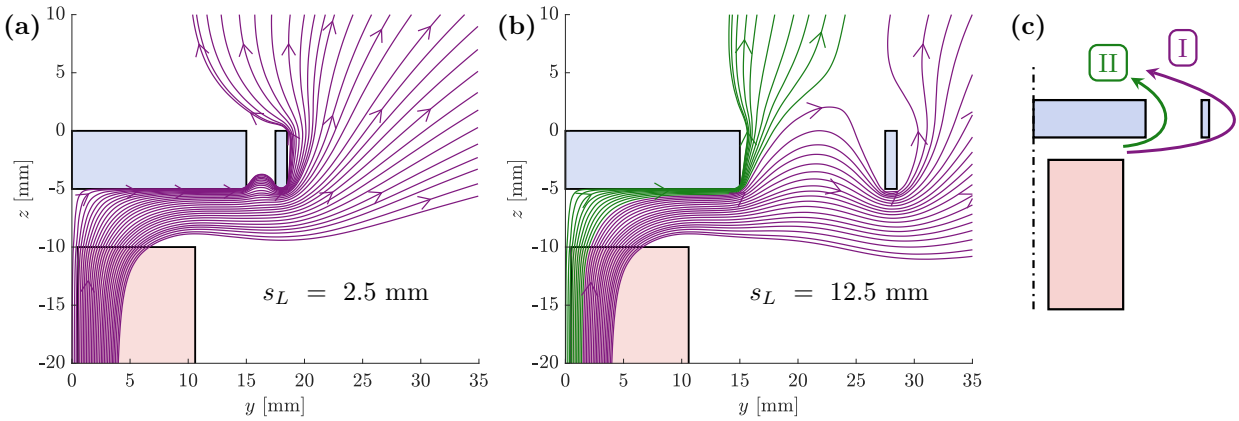

Figure 6. **(a)** Representation of the flux lines computed numerically for very small applied fields (around 1 mT at the bottom surface of the bulk). The coil is shown in red and the hybrid screen in blue. Only one loop is used and $s_L = 2.5$ mm. The flux lines are coloured depending on their path: I or II. **(b)** Same for $s = 12.5$ mm. **(c)** Schematic representation of the two possible paths followed by the flux lines reaching the region above the bulk.

screening properties. One of the main design rules is that an intermediate (sufficiently small) spacing should be chosen between the loops to maximize the usefulness of additional larger loops.

4. Experimental results and considerations

In the previous section, we discussed how the screening properties can be optimized by adjusting the geometric parameters of the screen. In this section, we explain how these improvements can be realized in practice. To this extent, the set-up described in section 2 is used. First, a large hybrid screen with four loop sizes is built. Then, the influence of the asymmetry of the loops, i.e. the vertical offset between both halves of the loops, is investigated.

Note that in all cases, only the results for the highest applied field, i.e. with 0.5 A in the coil, are shown. Several layers of closed-loop coated conductors are superimposed to increase the maximum current that can flow and ensure that the superconductors are weakly penetrated. In practice, SF is not observed to decrease when increasing the current from 0.1 to 0.5 A. Therefore, it is fair to assume that $\mu_0 H_{\text{app}} \ll \mu_0 H^*_{\text{app}}$ and, following the discussion of section 3, only the geometrical effects are discussed here.

One of the design rules of the finite element model was that, for an appropriate spacing s_L around 7.5 mm, increasing the number of loops improves significantly the screening properties. Hence, two configurations are compared experimentally: (i) a hybrid screen consisting of the 30 mm-diameter disk-shaped bulk with 45 mm- and 60 mm-diameter loops and (ii) a hybrid screen with the bulk and 45 mm-, 60 mm-, 75 mm- and 90 mm-diameter loops. These

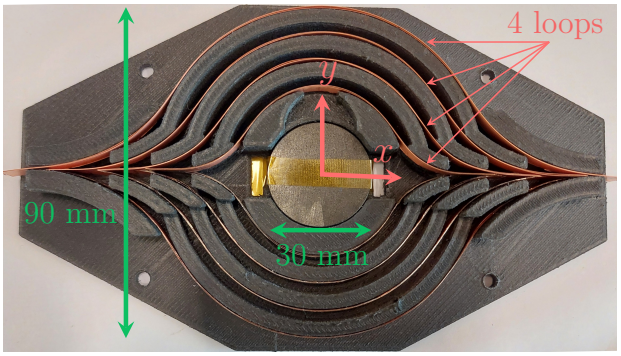

Figure 7. Picture of the hybrid screen consisting of a 30 mm-diameter bulk with 45 mm-, 60 mm-, 75 mm- and 90 mm-diameter loops. The screen is placed on a 3D-printed sample holder. All the loops are oriented in the same way: the upper part is at $y > 0$.

configurations correspond to a 7.5 mm spacing. All the loops are aligned in the same direction, with the upper part for $y > 0$, as shown in figure 7 for the second configuration.

Figure 8 shows the spatial distribution of SF along y, at $z = 5.7$ mm. The rectangles on the top of the graph show the region SF > 2, for $y < 0$. The results of figure 8 can be understood as follows.

First, by adding the two largest loops, the screened region extends up to $|y| \lesssim 48$ mm instead of $|y| \lesssim 33$ mm. This leads to a screened surface area approximately 2.2 times larger. Compared to the bulk alone [33], the screened surface area is ~ 9 times larger. Besides these numbers, the important point is that this process of adding loops is not intrinsically limited and can be used to build even larger screens provided that the spacing is appropriately chosen. The spacing

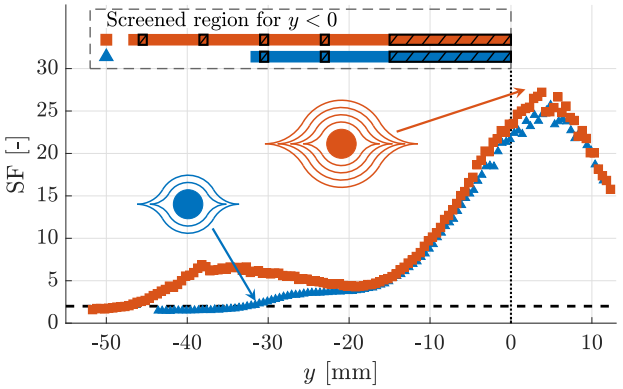

Figure 8. Spatial distribution of SF along y, for $z = 5.7$ mm. The blue triangles ▲ are for the screen made of a 30 mm-diameter disk-shaped bulk with 45 mm- and 60 mm-diameter loops. The red squares ■ are for the screen consisting of a 30 mm-diameter bulk with 45 mm-, 60 mm-, 75 mm- and 90 mm-diameter loops. The rectangles at the top of the graph indicate in each case the spatial extension of the region SF $>$ 2 for $y < 0$. The limit SF* $=$ 2 is shown by a dashed black line. The hatched black parts inside the coloured rectangles are located at the positions of the superconductors. The vertical dotted black line indicates the central position $y = 0$.

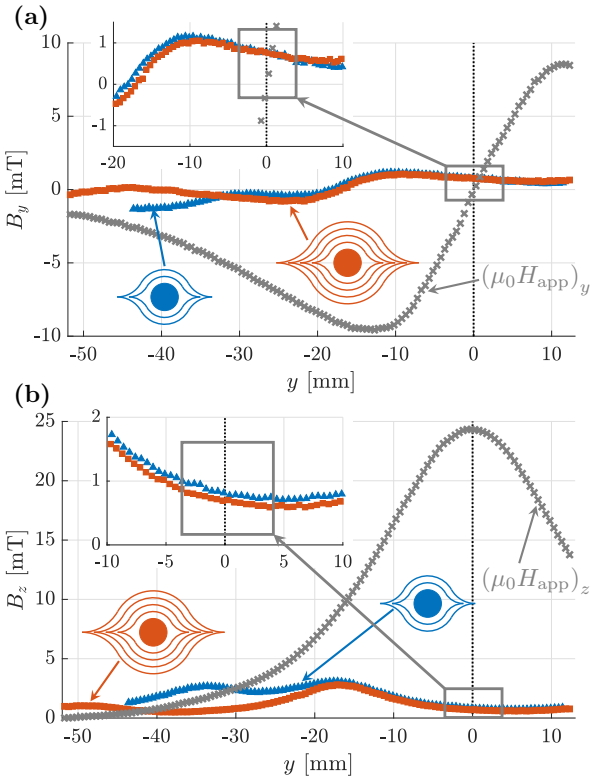

Figure 9. **(a)** Spatial distribution of B_y along y, for $z = 5.7$ mm. The y-component of the applied field in the absence of superconducting screen is shown with gray crosses ✕. The blue triangles ▲ are for the screen made of a 30 mm-diameter disk-shaped bulk with 45 mm- and 60 mm-diameter loops. The red squares ■ are for the screen consisting of a 30 mm-diameter bulk with 45 mm-, 60 mm-, 75 mm- and 90 mm-diameter loops. The dotted black line indicates the central position $y = 0$. **(b)** Spatial distribution of B_z along y, for $z = 5.7$ mm. The coloured symbols are the same as in **(a)**.

should be sufficiently small to avoid that too many flux lines leak through the gap between the bulk and the loops (see section 3.3). Such an appropriate spacing can be found for a given source coil with a simplified 2D model as figure 3.

Second, as mentioned previously, figure 5**(a)** shows a significant increase in the maximum modelled SF when comparing $N_L = 2$ (blue) and $N_L = 4$ (red) for $s_L = 7.5$ mm: SF at the centre rises from roughly 50 to 100. Such a large increase is not observed experimentally. This can be explained by taking into account the practical shape of the loops. The loops are not perfectly circular as assumed in the 2D finite element model but exhibit a vertical offset between both halves of the loop.

This asymmetry has two consequences that were described in our previous work [33]. First, the spatial distribution of SF at a given height $z > 0$ is not symmetric around $y = 0$. For $z > 0$, because of the offset between both halves of the loop, the distance to the loop for $y > 0$ is smaller than for $y < 0$ (see figure 7). Consequently, the opposite field generated by the supercurrents induced in the loops for $y > 0$ is larger than that generated for $y < 0$. Hence, SF is larger for $y > 0$. Secondly, the transverse component B_y is not zero around $y = 0$. The fact that $B_y(y = 0) > 0$ for $z > 0$ is again due to the vertical offset. This feature has a very detrimental effect on the measured screening properties, as shown in figure 9.

Figure 9**(a)** shows the spatial distribution of B_y at $z = 5.7$ mm. For $y = 0$, the inset illustrates that both configurations have $B_y \approx 0.8$ mT while the transverse component of the applied field is 0. Similarly, figure 9**(b)** shows the spatial distribution of B_z at $z = 5.7$ mm. It can be observed that $B_z(y = 0)$ is around 0.7 and 0.6 mT for 2 and 4 loops, respectively. Hence, adding more loops can reduce slightly B_z but cannot help reduce B_y, which is of the same order of magnitude. As a reminder, SF is computed as the ratio of the magnitude of the applied field and the magnitude of the measured flux density $\sqrt{B_x^2 + B_y^2 + B_z^2}$ (1). Therefore, this non-zero B_y is clearly a limiting term that prevents the SF from reaching high values (50 to 100) as predicted by the model.

Also, even if it is not the limiting factor in this case, it is worth mentioning that a large SF corresponds to a small field to measure, which may be limited by the uncertainty of the 3-axis Hall sensor, around 100 µT for the experimental set-up used in this work.

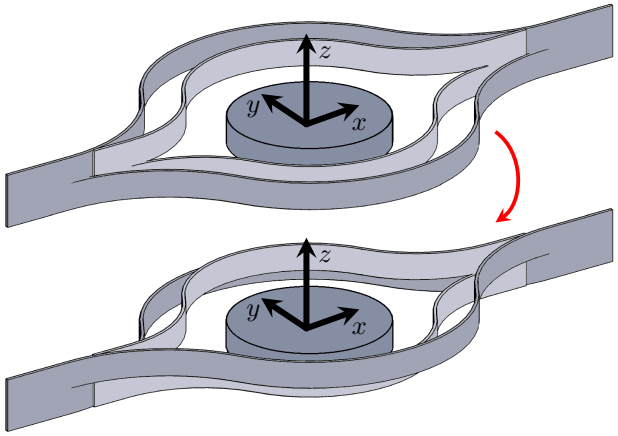

Figure 10. Schematic illustration of one way to reduce the transverse component B_y. Above: fully asymmetric configuration where both loops are oriented similarly. Below: 'symmetrized' configuration where one of the loops is flipped over.

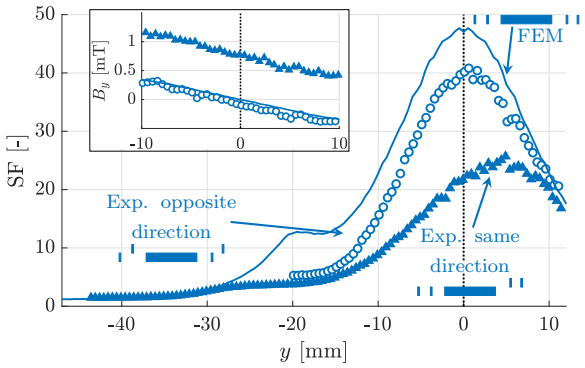

Figure 11. Spatial distribution of SF along y, for $z = 5.7$ mm. The blue triangles ▲ are for the screen made of a 30 mm-diameter disk-shaped bulk with 45 mm- and 60 mm-diameter loops in the same direction. The blue circles ○ are for the same screen but with the loops in opposite directions (see figure 10). The plain blue curve corresponds to the FEM results with $N_L = 2$ and $s_L = 7.5$ mm. The vertical dotted black line indicates the central position $y = 0$. The drawings show the cross-section of the different screens in the plane $x = 0$. The inset shows B_y around the centre in the same three cases.

Given the asymmetry of the loops, it is crucial to build screens that naturally minimize $|B_y|$ around the centre. The easiest way to achieve such a reduction is to reverse the direction of part of the loops used in the screen, as shown schematically for two loops in figure 10. This process can be extended to a larger number of loops. The point is that each additional loop should be added in a way that compensates as much as possible the asymmetry and the non-zero B_y around the centre.

The two configurations drawn in figure 10 were assembled and measured experimentally. The first consists of the bulk with 45 mm- and 60 mm-diameter loops oriented in the same direction (as it was the case in figure 8 and figure 9). The second one is the same except that the 60 mm-diameter loop is flipped over such that its upper part lies at $y < 0$. Figure 11 shows the spatial distribution of SF along y, at $z = 5.7$ mm. It can be observed that the screening properties are significantly improved for the 'symmetrized' configuration: the maximum SF increases from ~ 25 to ~ 41, which corresponds to a multiplication by roughly 1.6. Such an improvement is due to the reduction in $|B_y(y = 0)|$ which decreases from 0.8 mT to 0.1 mT, i.e. of the order of the typical uncertainty of the 3-axis Hall sensor, as shown in the inset of figure 11. It is worth emphasizing that this increase in SF does not require any supplementary superconducting material, it is a simple consequence of choosing appropriate orientations for the loops to minimize $|B_y|$.

In addition to the experimental data, figure 11 shows the results of the simplified 2D finite element model for $N_L = 2$ and $s_L = 7.5$ mm. Since the numerical model is axisymmetric (2D) while the experimental screen is not, a difference can be expected between the numerical results and the experimental data for the 'symmetrized' configuration. This can be noticed in figure 11; additional reasons for this discrepancy are that (i) the modelling of the coil is oversimplified with respect to the practical source coil, and (ii) the experimental results are prone to uncertainties (e.g. exact positioning or orientation of the Hall sensor). In spite of these expected discrepancies, the measured SF distribution for the configuration with opposite loop directions is now almost symmetric and satisfyingly closer to the results predicted by the simplified 2D finite element model.

5. Conclusion

In this work, we discussed how to design, improve and build practical hybrid high-temperature superconducting screens combining a disk-shaped bulk and closed-loop coated conductors placed coaxially. Ideally, these screens should provide (i) a strong field attenuation (ii) extending over wide surface areas and (iii) up to high inhomogeneous applied fields.

First, a simplified finite element model assuming axisymmetry allowed us to obtain a physical insight and some practical conclusions on the design of hybrid screens. Using large-J_c materials is a key element to increase the applied field up to which the screening properties are maintained. Simulations results suggest for example that multiplying J_c by 4 (e.g., by lowering the operating temperature) allows the screening properties to hold up to ~ 1 T. However, the screening properties (field attenuation and extension of the screened region) at low fields are limited by the geometry of the screen. Understanding

the different paths of the flux lines reaching the region above the screen is the best way to optimize the design of the screen by opposing at best all these paths. In general, an intermediate spacing is required for the screening properties to be scalable and to maximize the screening factor SF. Small closed-loop coated conductors allow for too many flux lines to meander around the screen and large closed-loop coated conductors allow for too many flux lines to leak through the spacing between the bulk and the loop. Importantly, the appropriate spacing leading to the maximum SF above the bulk can be found using a simplified axisymmetric model.

Then, we demonstrated how these large screens can be realized and optimized in practice, by performing experiments using GdBCO samples at $T = 77$ K with a DC inhomogeneous applied field around 100 mT at the bottom surface of the bulk. By using 4 closed-loop coated conductors spaced by 7.5 mm, the screened surface area (SF $>$ 2) was multiplied by ~ 9 with respect to a situation with the 30 mm-diameter bulk alone. Because the closed-loop coated conductors are asymmetric in practice, a non-zero transverse component is induced by the loops. This non-zero transverse component strongly limits the maximum SF that can be obtained above the screen. Hence, we proposed a 'symmetrized' configuration using two loops in which one of the loops is flipped over. This process can easily be extended to a larger number of loops. As a result, for a configuration using 2 loops, the maximum SF is multiplied by ~ 1.6 with respect to the situation with the loops oriented in the same direction. The resulting SF is also satisfyingly close to the prediction of the finite element model.

In summary, this work highlights three general design rules for building hybrid superconducting screens: (i) use large J_c superconductors, (ii) add several concentric loops with an appropriate spacing and (iii) reduce as much as possible any design asymmetry. Under specific temperature and external field conditions, these rules can always be used as a starting point for assembling more complex screens. In all cases, it is relevant to ensure that the superconductors are weakly penetrated, implement a simple numerical model and validate as soon as possible the design experimentally. Importantly, the general design rules presented in this work are therefore not strictly limited to a given source coil or an experimental set-up and can pave the way for the design of large screens in practical applications.

Data availability statement

All data that support the findings of this study are included within the article (and any supplementary files).

Acknowledgments

This work was supported by the Fonds de la Recherche Scientifique - FNRS under grant CDR n° J.0184.23. Nicolas Rotheudt is recipient of an FRS-FNRS Research Fellow grant. The work of Tomas Hlasek was supported by the Czech Science Foundation (project 24-10171S).

References

[1] Barna D 2017 *Phys. Rev. Accel. Beams* **20** 041002
[2] Capobianco-Hogan K, Cervantes R, Deshpande A, Feege N, Krahulik T, LaBounty J, Sekelsky R, Adhyatman A, Arrowsmith-Kron G, Coe B, Dehmelt K, Hemmick T, Jeffas S, LaByer T, Mahmud S, Oliveira A, Quadri A, Sharma K and Tishelman-Charny A 2018 *Nucl. Instrum. Methods Phys. Res. A* **877** 149–156
[3] Statera M, Balossino I, Barion L, Ciullo G, Contalbrigo M, Lenisa P, Lowry M, Sandorfi A and Tagliente G 2018 *Nucl. Instrum. Methods Phys. Res. A* **882** 17–21
[4] Barna D, Borburgh J, Atanasov M, Kirby G, Giunchi G, Kárpáti V, Szűcs M, Szabó G and Mertinger V 2022 *IEEE Trans. Appl. Supercond.* **32** 4000505
[5] Haran K S, Kalsi S, Arndt T, Karmaker H, Badcock R, Buckley B, Haugan T, Izumi M, Loder D, Bray J W, Masson P and Stautner E W 2017 *Supercond. Sci. Technol.* **30** 123002
[6] Haran K S, Loder D, Deppen T O and Zheng L 2016 *IEEE Trans. Appl. Supercond.* **26** 5202508
[7] Song X, Mijatovic N, Kellers J, Bührer C, Rebsdorf A V, Hansen J, Christensen M, Krause J, Pütz H, Wiezoreck J and Holbøll J 2017 *IEEE Trans. Appl. Supercond.* **27** 5201205
[8] Netter D, Leveque J, Ailam E, Douine B, Rezzoug A and Masson P 2005 *IEEE Trans. Appl. Supercond.* **15** 2186–2189
[9] Dorget R, Nouailhetas Q, Colle A, Berger K, Sudo K, Ayat S, Lévêque J, Koblischka M, Sakai N, Oka T and Douine B 2021 *Materials* **14** 2847
[10] Arpaia P, Ballarino A, Giunchi G and Montenero G 2014 *J. Instrum.* **9** P04020
[11] Bergen A A, van Weers H J, Bruineman C, Dhallé M M J, Krooshoop H J G, ter Brake H J M, Ravensberg K K, Jackson B D and Wafelbakker C K 2016 *Rev. Sci. Instrum.* **87** 105109
[12] Seidel P (ed) 2015 *Applied Superconductivity: Handbook on devices and applications* (Wiley)
[13] Wang Y, Wang Q, Wang H, Chen S, Hu X, Liu Y and Liu F 2021 *Supercond. Sci. Technol.* **35** 014001
[14] Jiles D 2015 *Introduction to Magnetism and Magnetic Materials* 3rd ed (CRC Press)
[15] Vant-Hull L L and Mercereau J E 1963 *Rev. Sci. Instrum.* **20** 418
[16] Claycomb J R and Miller J H J 1999 *Rev. Sci. Instrum.* **70** 4562–4568
[17] Pavese F 1998 Magnetic shielding *Handbook of Applied Superconductivity* ed Bristol: Institute of Physics Publishing pp 1461–83

[18] Rabbers J J, Oomen M P, Bassani E, Ripamonti G and Giunchi G 2010 *Supercond. Sci. Technol.* **23** 125003
[19] Fracasso M, Gömöry F, Solovyov M, Gerbaldo R, Ghigo G, Laviano F, Napolitano A, Torsello D and Gozzelino L 2022 *Materials* **15** 667
[20] Gozzelino L, Fracasso M, Solovyov M, Gömöry F, Napolitano A, Gerbaldo R, Ghigo G, Laviano F, Torsello D, Grigoroscuta M A, Aldica G, Burdusel M and Badica P 2022 *Supercond. Sci. Technol.* **35** 044002
[21] Fagnard J F, Elschner S, Bock J, Dirickx M, Vanderheyden B and Vanderbemden P 2010 *Supercond. Sci. Technol.* **23** 095012
[22] Denis S, Dusoulier L, Dirickx M, Vanderbemden P, Cloots R, Ausloos M and Vanderheyden B 2007 *Supercond. Sci. and Technol.* **20** 192–201
[23] Sasaki T, Tanaka M, Morita M, Miyamoto K M K and Hashimoto M H M 1992 *Jpn. J. Appl. Phys.* **31** 1026–1032
[24] Wéra L, Fagnard J F, Namburi D K, Shi Y, Vanderheyden B and Vanderbemden P 2017 *IEEE Trans. Appl. Supercond.* **27** 6800305
[25] Yang P, Fagnard J F, Vanderbemden P and Yang W 2019 *Supercond. Sci. Technol.* **32** 115015
[26] Zhang Z, Matsumoto S, Teranishi R and Kiyoshi T 2012 *Phys. Procedia* **27** 180–183
[27] Wu Y, Zhang G, Wu Y, Zhang D and Jing L 2023 *IEEE Trans. Appl. Supercond.* **33** 8800205
[28] Haseyama S, Fujinaka N, Yoshizawa S and Nakane H 2001 *Physica C Supercond.* **354** 437–440
[29] Terao Y, Sekino M, Ohsaki H, Teshima H and Morita M 2011 *IEEE Trans. Appl. Supercond.* **21** 1584–1587
[30] Douine B, Male G, Lubin T, Mezani S, Leveque J and Berger K 2014 *J. Supercond. Nov. Magn.* **27** 903–907
[31] Fagnard J F, Dirickx M, Levin G A, Barnes P N, Vanderheyden B and Vanderbemden P 2010 *J. Appl. Phys.* **108** 013910
[32] Wéra L, Fagnard J F, Levin G A, Vanderheyden B and Vanderbemden P 2015 *Supercond. Sci. Technol.* **28** 074001
[33] Rotheudt N, Brialmont S, Fagnard J F, Hlasek T, Plechacek J and Vanderbemden P 2024 *Supercond. Sci. Technol.* **37** 065008
[34] Hamilton W O 1970 *Rev. Phys. Appl.* **5** 41–48
[35] Motoki T, Yanai Y, Nunokawa K and Shimoyama J 2020 *Appl. Phys. Express* **13** 093002
[36] Motoki T, Sasada R, Tomihisa T, Miwa M, Nakamura S and Shimoyama J 2022 *Supercond. Sci. Technol.* **35** 094003
[37] Antončík F, Lojka M, Hlásek T, Sedmidubský D, Baumann J, Durrell J H, Cardwell D A and Jankovský O 2023 *J. Am. Ceram. Soc.* 2668–2678
[38] Levin G A, Barnes P N, Murphy J, Brunke L, Long J D, Horwath J and Turgut Z 2008 *Appl. Phys. Lett.* **93** 062504
[39] Lee H G, Kim J G, Lee S W, Kim W S, Lee S W, Choi K D, Hong G W and Ko T K 2006 *Phys. C: Supercond. Appl.* **445-448** 1099–1102
[40] Sheng J, Zhang M, Wang Y, Li X, Patel J and Yuan W 2017 *Supercond. Sci. Technol.* **30** 094002
[41] Zheng Y, Wang Y, Li J and Jin Z 2017 *AIP Adv.* **7** 095218
[42] Ali M Z, Zheng J, Huber F, Zhang Z, Yuan W and Zhang M 2020 *Supercond. Sci. Technol.* **33** 04LT01
[43] Zhao C, Shi J, Sheng J and Chen W 2022 *Crystals* **12** 1438
[44] Rotheudt N, Fagnard J F, Harmeling P and Vanderbemden P 2023 *Cryogenics* **133** 103693
[45] Nagasaki Y, Solovyov M and Gömöry F 2018 *IEEE Trans. Appl. Supercond.* **28** 1–5
[46] Life-hts: Liege university finite element models for high temperature superconductors `https://www.life-hts.uliege.be`
[47] Bossavit A and Verite J 1983 *IEEE Trans. Magn.* **19** 2465–2470
[48] Dular J, Geuzaine C and Vanderheyden B 2020 *IEEE Trans. Appl. Supercond.* **30** 1–13
[49] Sun J Z, Eom C B, Lairson B, Bravman J C and Geballe T H 1991 *Phys. Rev. B* **43**(4) 3002–3008